Materials Today Bio 28 (2024) 101204

Contents lists available at ScienceDirect

Materials Today Bio

journal homepage: www.journals.elsevier.com/materials-today-bio

Synthesis of hemostatic aerogel of TEMPO-oxidized cellulose nanofibers/collagen/chitosan and *in vivo/vitro* evaluation

Lu Liu [a,b,1], Liang Liu [b,1], Lin Chen [a], Genqiang Chen [a,b,**], Yen Wei [d], Feng F. Hong [a,b,c,e,*]

[a] State Key Laboratory for Modification of Chemical Fibers and Polymer Materials, Donghua University, Shanghai, 201620, China
[b] College of Biological Science and Medical Engineering, Donghua University, No.2999 North Ren Min Road, Shanghai, 201620, China
[c] National Advanced Functional Fiber Innovation Center, WuJiang, Suzhou, China
[d] Department of Chemistry and the Tsinghua Center for Frontier Polymer Research, Tsinghua University, Beijing, 100084, China
[e] Scientific Research Base for Bacterial Nanofiber Manufacturing and Composite Technology, China Textile Engineering Society, Shanghai, 201620, China

ARTICLE INFO

Keywords:
Nanocellulose
Hemostasis
Antibacterial activity
Electrostatic self-assembly
Sandwich structure
Collagen
Chitosan

ABSTRACT

The treatment of internal hemorrhage remains challenging due to the current limited antibacterial capability, hemostatic efficacy, and biocompatibility of hemostatic materials. The TEMPO-oxidized cellulose nanofibers/collagen/chitosan (TCNF/COL/CS) hemostatic aerogel was developed in this work by physically encasing COL in a sandwich structure and electrostatically self-assembling polyanionic TCNF with polycationic CS. *In vitro* coagulation experiments revealed the favorable procoagulant properties of TCNF/COL/CS along with high adhesion to erythrocytes and platelets. TCNF/COL/CS significantly increased the hemostatic efficacy by 59.8 % and decreased blood loss by 62.2 % in the liver injury model when compared to Surgicel®, the most frequently used hemostatic material. Furthermore, it demonstrated outstanding biodegradability both *in vitro* and *in vivo*, and a substantial increase in resistance (96.8 % against *E. coli* and 95.4 % against *S. aureus*) compared to TCNF. The significant hemostatic and biodegradable characteristics of TCNF/COL/CS can be ascribed to its interconnected porous structure, increased porosity, and efficient water absorption, along with the synergistic effect of the three constituents. The TCNF/COL/CS aerogel shows significant potential to control internal bleeding. A novel plant-derived nanocellulose composite aerogel has been described here for the first time; it has outstanding antibacterial characteristics, higher biocompatibility, and outstanding hemostatic characteristics *in vivo*.

1. Introduction

Hemorrhage is a major contributing factor to mortality. Internal hemorrhage constitutes a significant proportion of hemorrhagic mortality [1,2]. However, the inherent clotting mechanism of the body appeared to be inadequate in such critical conditions. This necessitates the incorporation of hemostatic materials in emergency medical and surgical procedures [3].

An optimal hemostatic substance would not only effectively prevent significant organ and arterial bleeding but also possess the advantageous characteristics of being antimicrobial, biocompatible, biodegradable, and cost-effective [4]. Bio-absorbable oxidized regenerated cellulose (ORC), is the commonly used substance to stop bleeding in surgical procedures. However, ORC still poses some significant challenges. The hemostatic efficacy of ORC is inadequate, particularly in patients with coagulopathies such as hemophilia [5]. The cytotoxicity of an excess of carboxyl groups in oxidized cellulose hinders the process of wound healing at lower pH and the antibacterial efficacy of ORC also remains constrained [6]. Therefore, a novel material is necessary to substitute the conventional ORC to address this issue.

Composite hemostatic materials are preferred over single-component products due to their high efficacy [7]. Wood-derived TEMPO-oxidized cellulose nanofiber (TCNF) possesses a high surface area and adequate carboxyl groups. While bacterial nanocellulose also possesses these characteristics, it is not as readily accessible. Consequently, TCNF is considered as a polyanionic nanocellulose with improved hemostatic properties and bioresorbability compared with conventional ORC. Chitosan (CS) polycationic demonstrates

* Corresponding author. State Key Laboratory for Modification of Chemical Fibers and Polymer Materials, Donghua University, Shanghai, 201620, China.
** Corresponding author. State Key Laboratory for Modification of Chemical Fibers and Polymer Materials, Donghua University, Shanghai, 201620, China.
E-mail addresses: chengenqiang@gmail.com (G. Chen), fhong@dhu.edu.cn (F.F. Hong).
[1] Contributions of both are equal.

https://doi.org/10.1016/j.mtbio.2024.101204
Received 16 February 2024; Received in revised form 4 August 2024; Accepted 13 August 2024
Available online 14 August 2024
2590-0064/© 2024 The Authors. Published by Elsevier Ltd. This is an open access article under the CC BY-NC license (http://creativecommons.org/licenses/by-nc/4.0/).

outstanding hemostatic properties *via* mechanisms distinct from oxidized cellulose. Furthermore, it possesses potent antibacterial potential, which can enhance the limited bactericidal capability of oxidized cellulose [8–10]. The TCNF/CS composite shows reduced cytotoxicity compared to the combined use of TCNF and CS, owing to its precisely balanced pH [11]. Collagen (COL) presents favorable hemostatic properties compared to oxidized cellulose and CS [12]. Moreover, favorable biocompatibility of COL may reduce the possible cytotoxicity of oxidized cellulose or CS [13]. Additionally, TCNF-based aerogels are simple to produce. These aerogels have the potential to provide effective hemostasis, superior biodegradability, and high absorption of wound exudate due to their high surface area and porosity [14–16]. However, there has been a scarcity of studies exploring the application of TCNF/COL/CS aerogel as a hemostatic substance.

In this study, TCNF/COL/CS hemostatic aerogel was developed to fulfill the needs of fast hemostasis, good biocompatibility, and effective antibacterial capabilities. Initially, a sandwich structure of TCNF/COL/CS aerogel was formed through the electrostatic self-assembly of polyanionic CS and polyanionic TCNF. COL was encapsulated in the aerogel during the assembly procedure (Fig. 1). The developed aerogel was characterized by its morphological, chemical, and physical properties. After that, the beneficial characteristics of TCNF/COL/CS aerogel were determined through *in vitro* evaluation of antibacterial, cytotoxic, hemostatic, and degradation properties. Furthermore, the efficacy and utility of TCNF/COL/CS were validated by *in vivo* assessments of hemostatic and degradation properties.

2. Material and methods

2.1. Materials

TCNF hydrogel (4.5 % aqueous slurry) was purchased from Zhongshan Naxiansi New Material Co., Ltd. Chitosan (M_W: 50000 Da; degree of deacetylation: approximately 85 %) was procured from Shanghai Yien Chemical Technology Co., Ltd. Collagen, extracted from fish skin, was purchased from Yuanye Bio-Technology Co., Ltd, while Surgicel® was developed by Johnson & Johnson Medical Co., Ltd. Gelatin sponge (Gelatin) was designed by Hushida Medical Technology Co., Ltd. Fibroblasts (L929) derived from mouse skin were purchased from the Institute of Biochemistry and Cell Biology, the Chinese Academy of Sciences. Cell Assay Kit was purchased from Beyotime Biotechnology Co., Ltd. Dulbecco's Modified Eagle's Medium (DMEM) and fetal bovine serum (FBS) were purchased from Life Technologies Co. Ltd. Rabbit blood was supplied by Suzhou Zhenhu Medical Technology Co., Ltd. Healthy Sprague Dawley (SD) rats were provided by Shanghai SLAC Laboratory Animal Co., Ltd. All animals were treated according to the Chinese National Institutes of Health Guidelines for Laboratory Animal Care and Use. All the experiments were performed by using deionized water (DW).

2.2. Preparing TCNF/COL/CS aerogel

A uniform suspension of TCNF 1 % (w/v) was prepared *via* dilution of 4.5 % TCNF slurry in DW. CS solution (1 % w/v) was prepared in 0.1

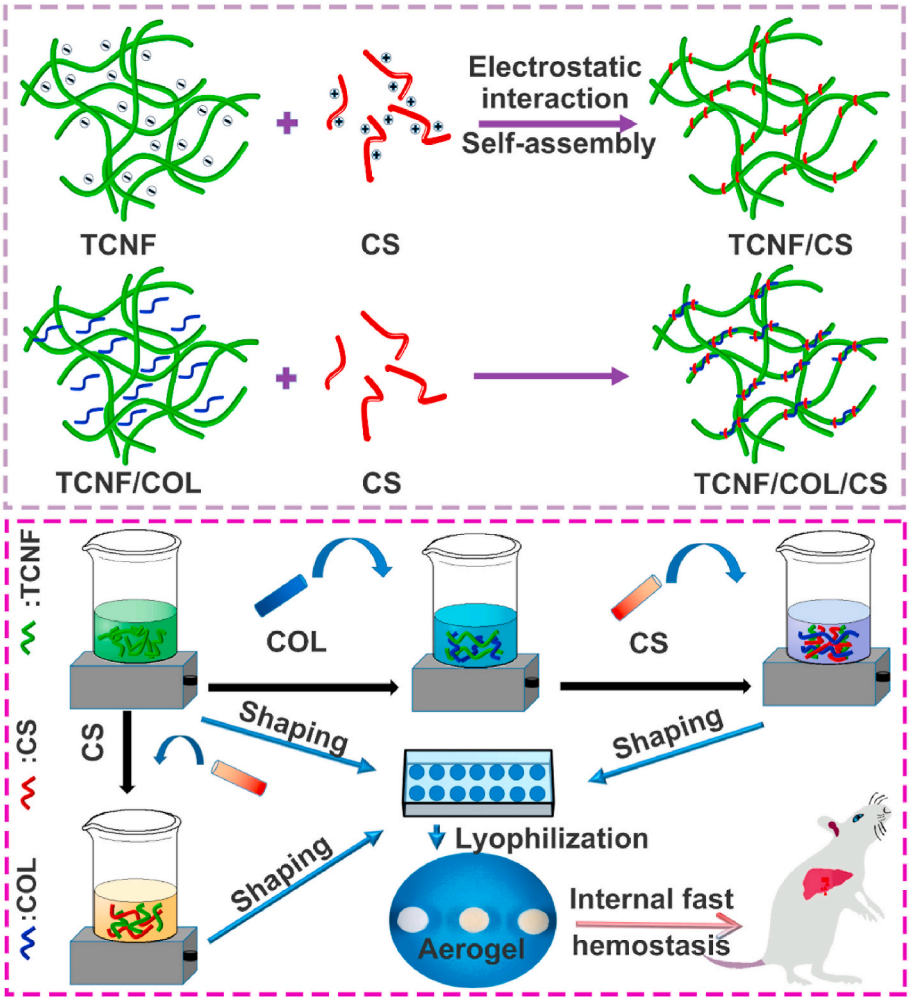

Fig. 1. A schematic representation of the synthesis of hemostatic aerogels.

M dilute acetic acid solution, then added dropwise into the aforementioned suspension of TCNF under vigorous agitation (Fig. 1). Preliminary experiments revealed that the TCNF/CS composite has a better tensile strength at the mass ratio of 1:1 for TCNF: CS (Fig. S5). The mass ratio of TCNF: COL: CS in this study was 1: 0.9: 1, which allowed for the highest loading of COL [6]. The pH of the final solution was adjusted to 6 by using 1 M NaOH. The precipitate was collected after repeated centrifugal washing to obtain a uniform suspension. The mixed solution was transferred into a mold, stored at −80 °C for 12 h, and freeze-dried for 48 h. TCNF/CS composite was prepared using the same procedure.

2.3. Characterization of the physicochemical properties of the aerogel

The microstructure of lyophilized aerogel was investigated using the field emission scanning electron microscope (FE-SEM, Hitachi) [17] while the determination of its chemical composition was carried out using Fourier Transform Infrared Spectroscopy (FTIR) [18]. The Thermogravimetric Analyzer (209 F3 Tarsus®) was used to conduct the thermogravimetric (TG) analysis [19]. The ζ-potential was measured through the Zetasizer Nano ZS instrument (Malvern) [20]. The density of the sample was determined by using mass-volume analysis. Results for water absorption capacity and porosity examination were in agreement with those of previous studies [21,22]. The Surgicel® (weft-knitted fabric) porosity test was not conducted since it does not fulfill the ethanol filling pore criteria.

A universal testing machine with a speed of 3 mm/min was used to record the compression performance of the aerogel (diameter: 10 mm; thickness: 10 mm) both before and after water absorption. At least 6 replicates were performed for each sample.

2.4. Cytotoxicity assay

In 48-well plates, cells were directly treated with both the samples and the Surgicel® (control). Cell suspensions (1×10^4 cells) in DMEM medium with 10 % (v/v) FBS and 1 % (v/v) penicillin-streptomycin solution were added to the 48-well plates and incubated for 5 days under 5 % CO_2 at 37 °C. The CCK-8 assay was used to determine cell viability (n = 3), while the morphology of the cells was determined using Calcein AM assay reagents [23,24]. In order to assess the cellular behavior on the materials on Day 5, the samples were fixed in 2.5 % glutaraldehyde, dehydrated in ethanol, freeze-dried, and then examined *via* FE-SEM.

2.5. Determination of hemocompatibility

The samples were assessed for whole-blood coagulation, erythrocyte adhesion, and platelet adhesion using previously described procedure [25]. The analysis of whole blood coagulation was performed by adding 0.025 M $CaCl_2$ (500 μL) into 5 mL of whole blood to induce coagulation. Activated blood (100 μL) was evenly distributed onto the samples in a 24-well plate and incubated at room temperature for different time intervals (5, 15, 25, 35, 45, 55 min). Following each time point, 2.0 mL of ultrapure water was introduced into the wells and incubated for 5 min to lyse non-thrombus-trapped red blood cells. The resulting suspension (200 μL) from each sample was transferred to a 96-well plate; absorbance was recorded at 540 nm using a microplate reader for the determination of hemoglobin content. The hemolytic ratio experiment comprised various steps. The whole blood was initially centrifuged for 10 min at 100 g. The platelet-rich plasma (PRP) comprised the upper suspension, whereas red blood cells (RBCs) comprised the lower layer. RBCs were diluted with normal saline to a 5 % (v/v) solution. DW and normal saline served as positive and negative controls, respectively. After that, suspensions of varying concentrations (0.625, 1.25, and 2.5 mg/mL) are prepared by combining powdery aerogel with normal saline. In tubes, RBC suspension and solution were combined in equal volumes and incubated at 37 °C for 1 h. All the samples were centrifuged (116 *g*, 10 min), and the absorbance was recorded at 540 nm using a microplate reader [21]. Each sample was examined three times. The hemolytic ratio was calculated using the following equation:

$$\text{Hemolytic ratio}\ (\%) = (OD_s - OD_n) \ / \ (OD_p - OD_n) \times 100 \quad (1)$$

where OD_s, OD_p, and OD_n are the values of the aerogel, positive control, and negative control, respectively. Each sample was measured in triplicate.

2.6. In vivo hemostatic assay

The hemostatic performance of the aerogel was evaluated using liver trauma model of male rats (300–400 g). The rats were divided into four groups (n = 10/group) and anesthetized with 10 % chloral hydrate solution. The livers of the mice were exposed after they were fixed. A 3 mm deep liver injury was created, and a pre-weighed sample (diameter: 10 mm; thickness: 5 mm) was applied to the bleeding site. The absorbed blood sample was weighed and the hemostasis time was recorded.

2.7. Evaluation of antibacterial properties

The antibacterial activity of the samples was evaluated against *Escherichia coli* (*E. coli*) and *Staphylococcus aureus* (*S. aureus*) using ISO 20743-2007 standard absorption method [26]. Samples were inoculated with a bacterial concentration (1×10^5 to 3×10^5 cfu/mL) and incubated for 24 h. After incubation, the samples were washed with 10 mL of a medium to remove the bacteria, followed by quantification using spread plating. Each sample was examined three times, and cotton gauze served as the control for the experiment.

2.8. In vitro and in vivo degradation behavior

The sample (30 mg) was soaked in PBS (pH 7.4) and incubated at 37 °C for specific durations. The mixture was then dialyzed and washed for 48 h followed by lyophilization and weighing (W_1). The degradation rate was calculated as follows:

$$\text{Degradation ratio}\ (\%) = (W_1\text{-}W_0) \ / \ W_0 \times 100 \quad (2)$$

where W_0 represents the original weight of samples.

Male rats were used to analyze the *in vivo* degradation behavior. The rats were divided into four groups (n = 10/group). The rats were anesthetized and subcutaneously implanted with sterilized samples (diameter: 15 mm, thickness: 5 mm). The materials were surgically removed together with the surrounding tissues after 1 and 4 weeks. Observable stained sections were obtained after the treatment.

All the animal involved experiments were approved by the Laboratory Animal Ethics Review Committee of Donghua University (DHUEC–NSFC–2019-13). All the experiments were performed following ethical standards and the Guide for the Care and Use of Laboratory Animals (Ministry of Science and Technology of China, 2006).

2.9. Statistical analysis

Statistics were expressed as the mean ± standard deviation. Statistics were expressed as the mean ± standard deviation. For the experimental data among groups, one-way ANOVA with Tukey's post hoc test was used. $P < 0.05$ indicated significant differences.

3. Results and discussion

3.1. Morphological analysis

The SEM images of aerogels are shown in Fig. 2 demonstrating that all the sponges displayed a uniform and interconnected porous structure. Nanopores were formed by the process of low-temperature cooling,

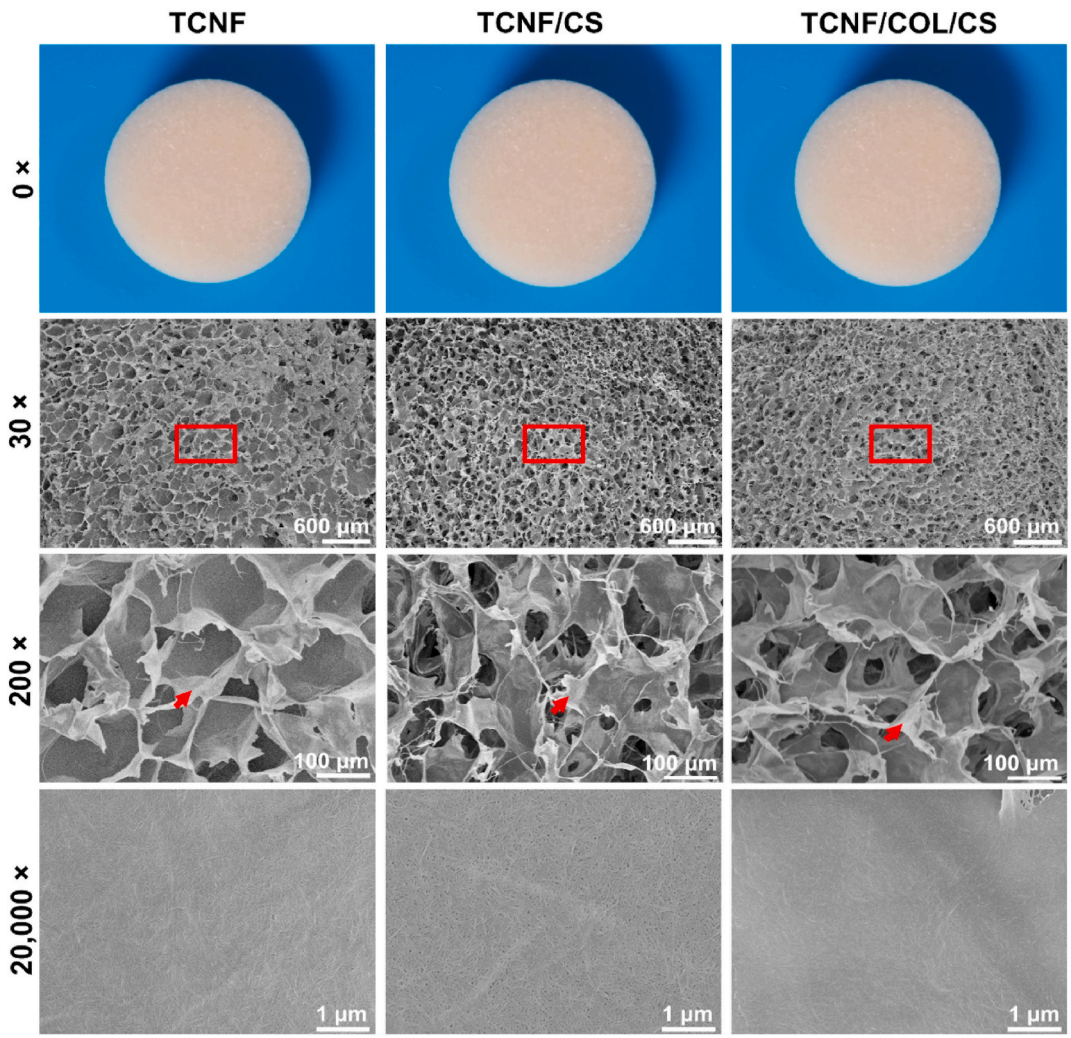

Fig. 2. The surface morphology of the aerogel samples at different magnifications. The red box and arrow represent the enlarged area and position, respectively.

during which the material became confined around growing ice crystals. Following the removal of the ice *via* freeze-drying, porosity was generated. TCNF showed a three-dimensional sheet-like structure formed by interweaving nanofibers. In contrast to TCNF, the TCNF/COL/CS and TCNF/CS structures were loose and disorganized with a higher number of smaller holes. Nano-scale pores appeared between TCNF fibers in the SEM image at 20,000 × ; the pores became larger following the coupling of CS. This can be attributed to the separation of the TCNF nanofibers, which were previously interconnected *via* hydrogen bonds, during the electrostatic self-assembly process involving CS and TCNF. Nearly all holes in TCNF/COL/CS become smaller upon the addition of COL, indicating an even denser structure. SEM images demonstrated the successful preparation of TCNF, TCNF/CS, and TCNF/COL/CS aerogels with distinct microstructure.

The nanocellulose-based aerogels developed in this study demonstrated a considerably greater porosity (Fig. 2) when compared to the commonly employed hemostatic material of Surgicel®, an ORC-prepared weft-knitting fabric product [27,28]. Furthermore, the aerogel showed a porous structure that closely resembled the extracellular matrix [29]. This characteristic may potentially facilitate the rapid absorption of liquids, increase the surface area in contact with blood, stimulate blood coagulation components, and support blood coagulation throughout the coagulation process [14,30].

3.2. Analysis of physicochemical properties

The TCNF/COL/CS aerogels were analyzed for their physicochemical parameters, including chemical composition, thermal stability, density, surface charge, porosity, and water absorptivity (Fig. 3). The FT-IR spectra of TCNF/COL/CS aerogels and other materials are shown in Fig. 3A. The TCNF spectrum displayed a prominent peak at approximately 1050 cm^{-1}, corresponding to the skeletal vibration of the C–O–C pyranose ring [31]. Furthermore, the peak observed at 1606 cm^{-1} suggests the presence of carboxyl groups [32], while CS showed two distinct peaks at 1646 and 1585 cm^{-1}, corresponding to the amide I (1641-1646 cm^{-1}) and amide II (1585 cm^{-1}), respectively [33,34]. The compound COL showed absorption peaks at 1640 and 1540 cm^{-1}, which can be ascribed to the stretching vibration of the C=O bond in the peptide group (amide I) and bending vibration of the N–H bond (amide II), respectively [35]. There were discernible peaks in the TCNF/CS and TCNF/COL/CS spectra that corresponded to the cellulose pyranose ring, amide groups, and carboxyl groups. Meanwhile, these characteristic peaks demonstrated a shift in wave number with change in intensity in the spectrum of TCNF/CS and TCNF/COL/CS. The –COO– peaks of TCNF/CS and TCNF/COL/CS were shifted from 1606 cm^{-1} (in TCNF) to 1546 and 1539 cm^{-1}, respectively. The shifting of amide I peak was observed from 1646 cm^{-1} (CS) to 1631 and 1630 cm^{-1} in TCNF/CS and TCNF/COL/CS, respectively. The red shift of –COO– peaks indicated the electrostatic interactions between TCNF and CS [36,37] while the red shift of amide I in TCNF/CS and TCNF/COL/CS indicates that CS has

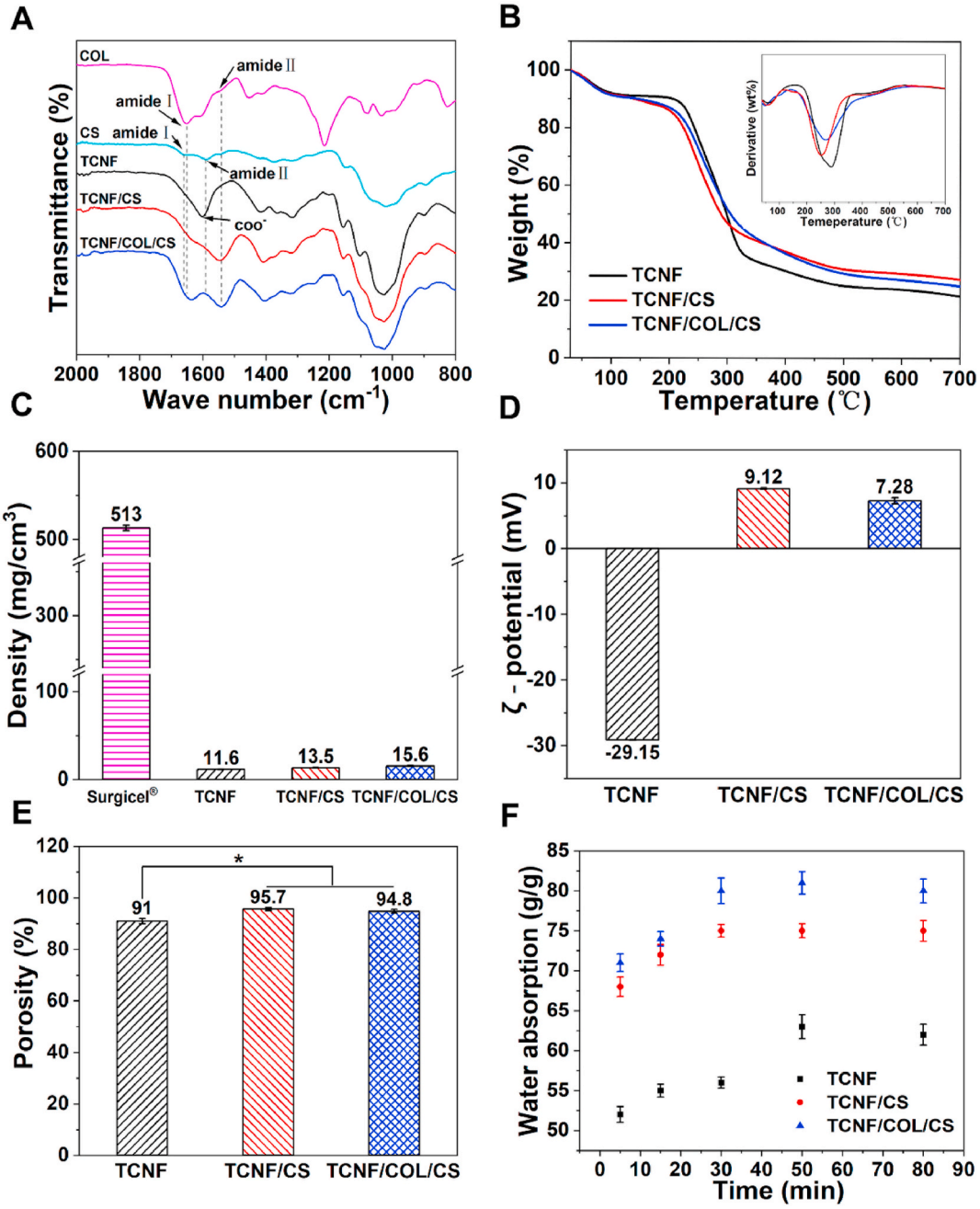

Fig. 3. (A) FT-IR. (B) TG and DTG of composites. (C) Density of the samples. (D) ζ-potential. (E) Porosity and (F) water absorption capability of aerogels. (*$p < 0.05$).

been successfully incorporated into the composites [33]. Moreover, TCNF/COL/CS spectrum showed a significantly higher peak intensity at 1540 cm^{-1} compared to the TCNF/CS, indicating the incorporation of COL into the aerogel [38]. The results of the spectrum analysis show that the TCNF/CS and TCNF/COL/CS composites were successfully synthesized. The TG analysis (Fig. 3B) showed the stability of TCNF/COL/CS at room temperature.

Fig. 3C displays the density of the samples showing the value of 513, 11.6, 13.5, and 15.6 mg/cm^3 for Surgicel®, TCNF, TCNF/CS, and TCNF/COL/CS respectively. The density of these TCNF-based composites was comparable to that of conventional aerogel (0.1–200 mg/cm^3) [39]. The density of TCNF/COL/CS and other TCNF-based materials was determined to be 97 %–97.7 % lower than that of Surgicel®. Comparatively, the density of TCNF/COL/CS was significantly lower than that of nanocellulose-based biomaterials reported in the literature [40,41]. With an aldehyde content of 17.93 %, the CNF/COL aerogel created by Lu et al., had a density of 20.6 mg/cm^3 and exhibited exceptional biocompatibility [41].

The ζ-potential (Fig. 3D) of the aerogels TCNF, TCNF/CS, and TCNF/COL/CS were observed as −29.15, 9.12, and 7.28 mV, respectively. The difference between TCNF and TCNF/CS may be associated with the comparatively higher concentration of $–NH_4^+$ present in polycationic CS compared to the TCNF -COO^-. The charge of TCNF/COL/CS was 1.84 mV lower than that of TCNF/CS which may be attributed to the shielding of $–NH_4^+$ by the adsorption of COL.

The porosity of the aerogels is shown in Fig. 3E. A higher level of porosity was observed in TCNF/CS (95.7 %) and TCNF/COL/CS (94.8 %) as compared to TCNF (91 %). The incorporation of CS into the TCNF network increased the porosity of TCNF/CS, which was subsequently reduced following the addition of COL. The SEM image (Fig. 2) provides evidence that TCNF becomes fluffy after being combined with CS and demonstrates various interconnected small pores. The porosity of TCNF/

COL/CS observed in this study was considerably higher compared with previous research [30,42]. According to the study conducted by Sukul et al., the porosity of the TCNF/CS composite material was found to be 67.2 % [42], which was 27.6 % lower than the porosity of the TCNF/COL/CS aerogel.

Fig. 3F shows the water absorption capability of TCNF, TCNF/CS, and TCNF/COL/CS showing the potential to absorb 52, 68, and 71 g/g of DW in 5 min. On the other hand, Surgicel® hardly swells after soaking in water. The TCNF/COL/CS material showed the highest water absorption capability, reaching saturation within 30 min. The TCNF/COL/CS water absorption rate altered by 12.3 % after 5 min, whereas the TCNF/CS rate changed by 9.3 %. However, the TCNF reached saturation after 50 min. The high water absorption capacity of the TCNF aerogel can be attributed to its high porosity, which facilitates the rapid permeation of water molecules *via* the interconnected pores and regular 3D structure of the aerogel (Fig. 2). Conversely, the water absorption capacity was further increased due to the disruption of the hydrogen bond between TCNF caused by the incorporation of CS [43]. The rapid and extensive water absorption capability of TCNF/COL/CS establishes a theoretical basis for the phenomenon of rapid hemostasis. The present study observed that TCNF/COL/CS displayed an extremely high water absorption rate when compared to other materials of a similar nature [44,45]. The water absorption capacity of the TCNF/COL/CS composites was 35 g/g higher than that of composites proposed by Liu et al., which comprised quaternary ammonium salt conjugated CS (QAS-CS), polyacrylate (PAAS), and COL [44].

3.3. Mechanical properties

The mechanical properties of the dry aerogel and the aerogel in the swollen state are shown in Fig. 4. The compression strength of TCNF/CS in dry aerogels was determined to be slightly lower than that of TCNF under various deformation conditions. The inclusion of COL further reduced the compression strength. The compression modulus of the dry aerogels decreased in the following order: TCNF (157 kPa) > TCNF/CS (110 kPa) > TCNF/COL/CS (97 kPa). The mechanical strength of swollen materials was improved by the addition of CS or COL, in contrast to dry aerogels; however, the overall mechanical strength decreased after swelling (Fig. 4B and D). The modified TCNF showed the most unfavorable mechanical parameters (1.44 kPa for compression strength at 80 % deformation and 3.24 kPa for compression modules). The network formed by combining CS and TCNF increased the

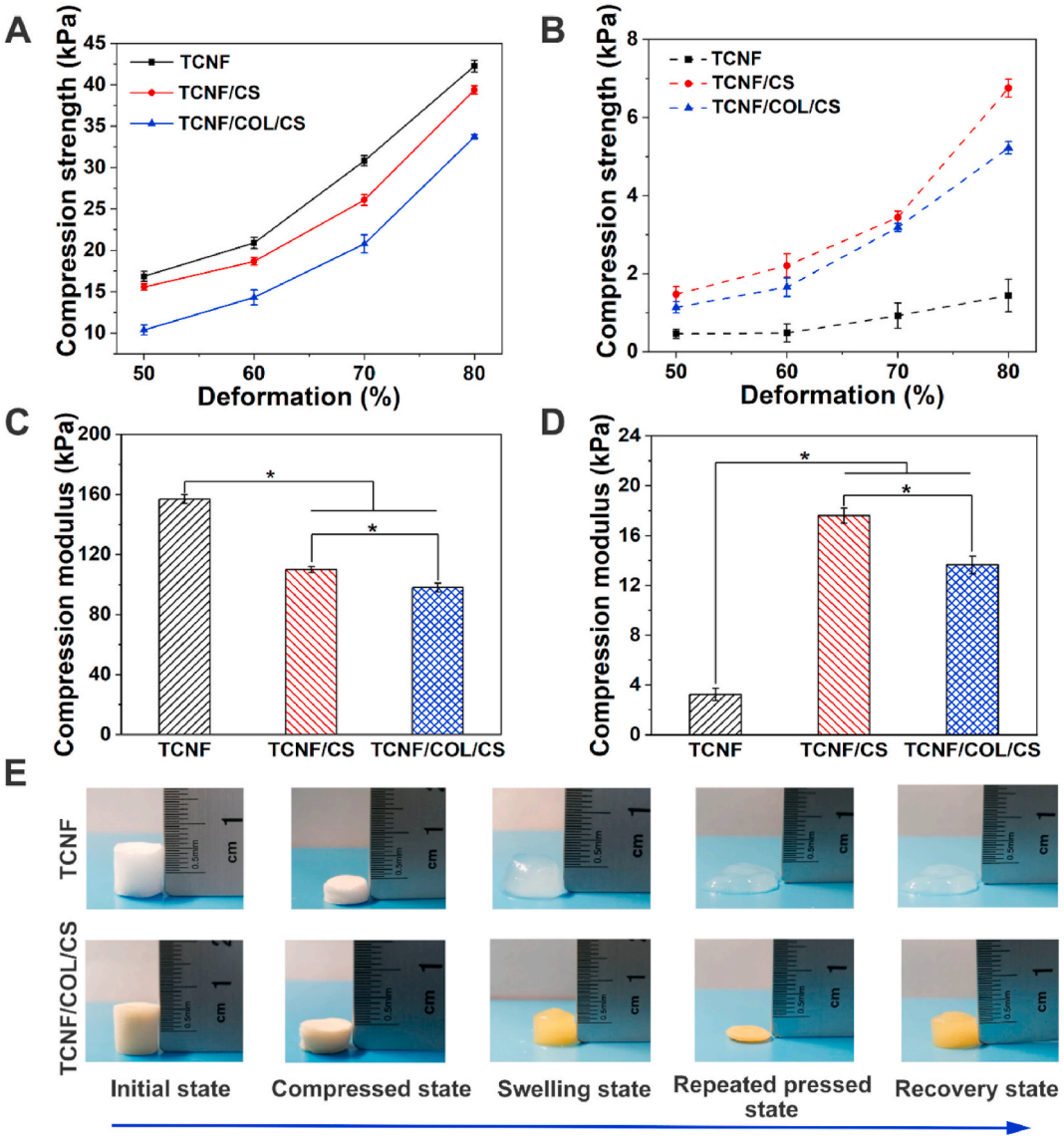

Fig. 4. The mechanical properties of various samples. The compression strength of dry (A) and swelling samples (B) under different deformations. The compression modulus of dry (C) and swelling samples (D). (E) Recovering TCNF and TCNF/COL/CS through water absorption in various shapes. (*p < 0.05).

compressive strength of TCNF/CS by 88.2 % resulting in an approximately 6-fold increase in the compressive modulus. In contrast to pure TCNF, the TCNF/COL/CS composite showed a considerably enhanced strength profile, as evidenced by a 72.5 % rise in compressive strength and an 86.3 % change in compressive modulus ($p < 0.05$). Fig. 4E shows that water absorption caused the TCNF structure to become loose and repetitive pressing was unable to preserve the aerogel shape. Conversely, repeated pressing of TCNF/COL/CS resulted in the restoration of its original shape.

The observed decrease in compression strength and modulus of compression in dried samples can be ascribed to the presence of CS, which disrupts the strong hydrogen bonding between TCNF. The SEM image (Fig. 2) also revealed that the overall structure had become less compact after the incorporation of CS. The interaction between carboxyl groups on TCNF and COL, which subsequently influences the formation of ionic bonds during electrostatic adsorption, may account for the decrease in compression strength caused by COL in dry samples (TCNF/COL/CS). The addition of CS disrupts the hydrogen bonds between TCNF during the process of swelling. Nevertheless, ionic interactions offer another kind of interaction between TCNF and CS that contributes to maintaining and enhancement of mechanical strength [6]. Therefore, the inclusion of CS and COL in the dry state was associated with a decrease in compression strength, whereas their presence in the swollen state resulted in an increase in compression strength. The recovered property may be associated with the intersection of TCNF induced by COL and CS [46,47].

3.4. Cytotoxic activity

Cytotoxic behavior of the Surgicel® and these TCNF-based aerogels was investigated in terms of cell morphology, cell viability, and cell proliferation (Fig. 5). An increase in the cell count was observed on these TCNF-based aerogel surfaces while Surgicel® maintained nearly constant cell counts for five days (Fig. 5A). L929 cells showed consistent

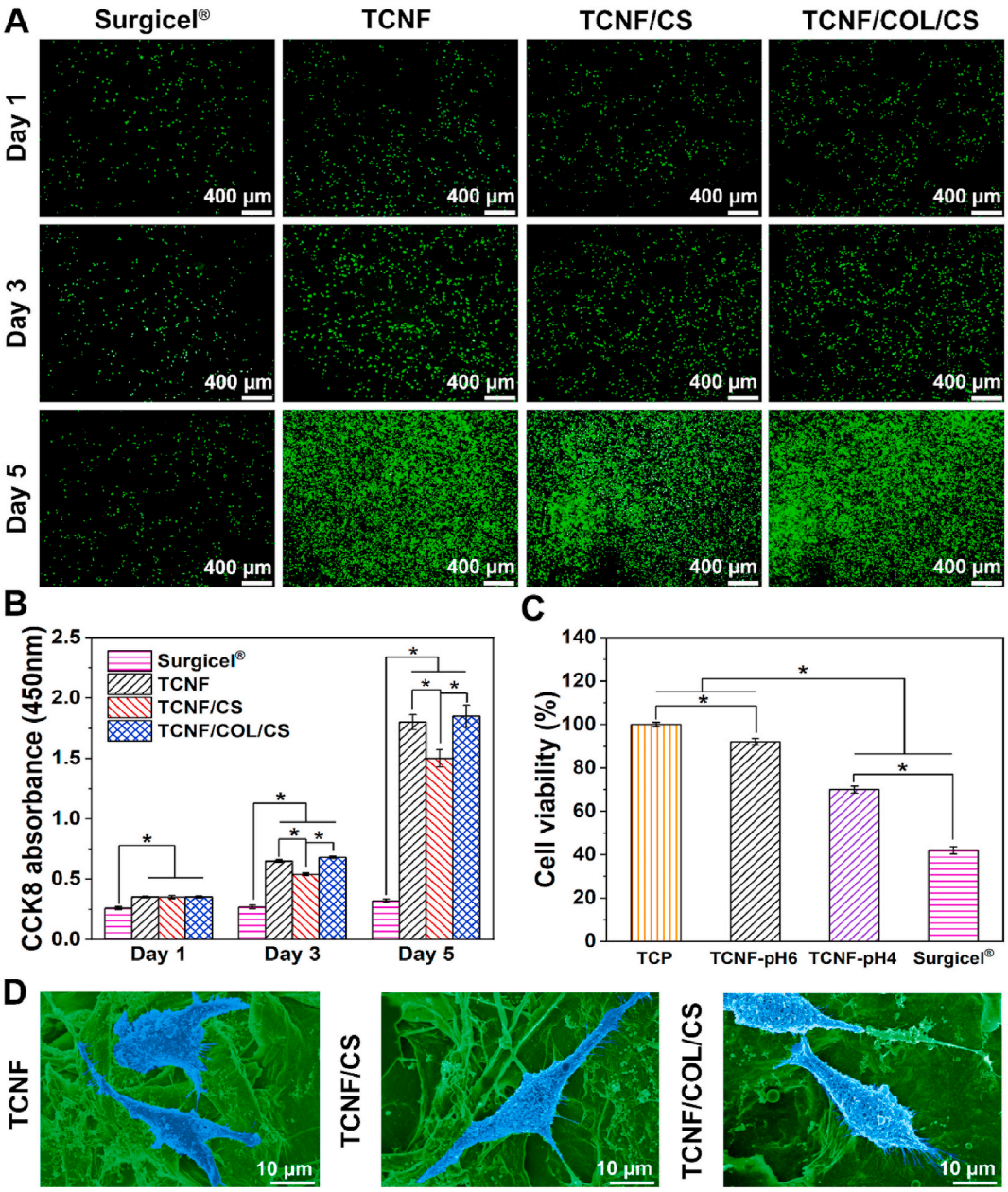

Fig. 5. (A) Images of Calcein AM-stained fibroblasts cultivated with samples. (B) Numbers of cells cultured on the samples. (C) Cell viability for 3 days at various pH. (D) The cytocompatibility of samples was examined by SEM. (*$p < 0.05$).

proliferation on TCNF, TCNF/CS, and TCNF/COL/CS throughout the incubation period of five days (Fig. 5B). Compared to Surgicel®, TCNF, and TCNF/CS, the proliferation rate of TCNF/COL/CS was significantly higher ($p < 0.05$) on Days 3 and 5. The absorbance of TCNF/COL/CS increased by 82.7 % on Day 5, compared with the Surgicel®. Cell viability was assessed on Day 3 after treatment with TCNF-pH 6, TCNF-pH 4, and Surgicel® samples (Fig. 5C), and the results revealed the respective cell viability of 92, 70, and 42 %. The cell morphology of TCNF, TCNF/CS, and TCNF/COL/CS revealed the presence of L929, as illustrated in Fig. 5D. The samples displayed a distinctive cellular morphology of fibroblasts on the TCNF/COL/CS, which was distinguished by the formation of stretched-out pseudopodia and spindles.

The enhanced cytocompatibility of TCNF/COL/CS can be attributed to its favorable properties that facilitate cell growth, such as an appropriate pH (Fig. 5C), a matrix provided by an aerogel structure with a larger specific surface area (Fig. S3), significant porosity (Fig. 3E), and permeability (Fig. 3F) [14,29]. Moreover, the incorporation of COL and CS in TCNF/COL/CS has the potential to improve cell proliferation [48]. Fibroblast proliferation was observed across all aerogels, as illustrated in Fig. 5B. The growth of fibroblasts was found to be more favorable on TCNF/COL/CS that contained complete nanopores. It was found that materials with a pH of 6 promoted cell development more effectively [49]. According to the report, the pH of ORC is around 3.1. Cytotoxicity of Surgicel® (Fig. 5C) may be attributed to the carboxyl groups' contribution to an acidic environment, which is detrimental to cell growth [50].

The cytocompatibility of the aerogel TCNF/COL/CS is preferable to that of similar composites proposed by other researchers [48,51]. Fluorescent cell staining in a study on COL/CS porous material cross-linked with glutaraldehyde confirms that COL/CS can reduce the toxicity induced by the cross-linking agent, thereby providing the material with higher biocompatibility [48].

3.5. *In vitro* hemocompatibility

Various parameters were used to evaluate hemocompatibility, including the morphology of platelets and erythrocytes, absorptivity of whole blood, and coagulation rate of whole blood (Fig. 6). The hemolysis ratio of TCNF, TCNF/CS, and TCNF/COL/CS was determined to be <1 % (Fig. 6A). The concentration and absorption capabilities of samples in relation to whole blood are illustrated in Fig. 6B. The gelatin sponge displayed the presence of free-floating blood beads, whereas TCNF/COL/CS and other substances rapidly absorbed blood. The blood could be concentrated more rapidly using the aerogels TCNF/CS and TCNF/COL/CS compared with Surgicel® and TCNF. Gelatin aerogel showed the lowest procoagulant activity, followed by Surgicel®, as demonstrated in the blood coagulation experiment (Fig. 6C). The highest ranking was achieved by TCNF/COL/CS in whole-blood coagulation. Absorbance values of 1.74, 1.18, 1.02, 0.54, and 0.41 were determined in the groups containing Gelatin, Surgicel®, TCNF, TCNF/CS, and TCNF/COL/CS, respectively, after 5 min.

After that, morphological analysis of platelets and erythrocytes on these materials was carried out by using SEM (Fig. 6D). In comparison to Gelatin, Surgicel®, and TCNF, TCNF/CS and TCNF/COL/CS showed a significantly higher platelet adhesion capability. Moreover, the platelets on TCNF/COL/CS stretched spiny pseudopods to interweave and form spongy undulating platelet clusters. Similarly, Gelatin, Surgicel®, and TCNF showed decreased RBC adherence, allowing RBCs to retain their typical biconcave shape. Conversely, erythrocyte adhesion was significantly increased in TCNF/CS and TCNF/COL/CS, leading to irregular morphology and aggregation.

The increased hemocompatibility of TCNF/COL/CS aerogel *in vitro* can be attributed to its bioactive components, optimal physicochemical characteristics (as shown in Fig. 3), and higher cytocompatibility (Fig. 5). The aerogels possess a significant level of porosity (Fig. 3E), a high water-absorbing capacity (Fig. 3F), and a porous structure (Fig. 2). These characteristics enable them to rapidly absorb blood and

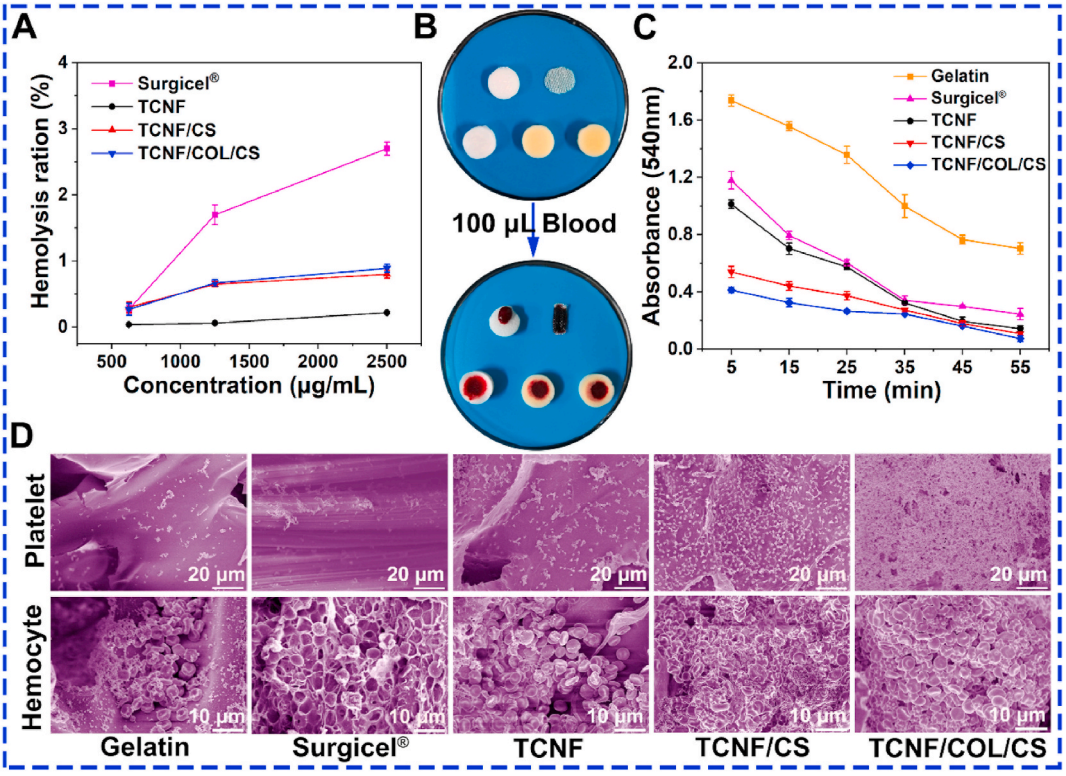

Fig. 6. *In vitro* hemolytic activity and blood-clotting capability of samples. (A) Hemolysis ratio of the samples. (B) The ability of samples to concentrate blood. (C) Analysis of samples using dynamic whole-blood clotting. Adherence of platelets and erythrocytes to the materials was observed in SEM images (D).

concentrate clotting components [52]. Therefore, TCNF/COL/CS showed a low absorbance value during the initial phases of the blood coagulation experiment (Fig. 6C). The increased specific surface area (Fig. S3) of TCNF/COL/CS allowed for enhanced interaction between the components in the blood, hence accelerating the binding of various components such as CS, COL, RBCs, and platelets. The positively charged $-NH_4^+$ groups present in the CS resulted in a significant attraction of a large number of RBCs, leading to their aggregation into clusters [53]. Furthermore, the incorporation of COL into TCNF/CS improved its coagulation capacity by stimulating platelets, thereby facilitating their aggregation.

The *in vitro* performance of TCNF/COL/CS was found to be superior in comparison with other potential hemostatic materials. The TCNF/COL/CS aerogel material exhibited a hemolysis ratio being less than 1 %, positioning it as a superior hemostatic material [30,54]. CS-based nanomaterial has also been reported to have a low hemolysis ratio, with approximate value of 1.24 % [54]. Conversely, in comparison to other cellulose-based hemostatic materials, TCNF/COL/CS demonstrated enhanced blood absorptivity and blood coagulation rate. the absorbance of TCNF/COL/CS consistently remained below 0.5 throughout the coagulation process, which was lower than the midpoint or end point of coagulation observed in previous studies [6,55]. The absorbance of the coagulation starting point of the hemostatic material (OBC/DFO), which comprised deferoxamine (DFO) and oxidized bacterial cellulose (OBC), was determined to be > 2. After 9 min, the absorbance reached the value of 0.5 [55]. Furthermore, the initial coagulation absorbance of OBC/COL/CS was significantly higher than 0.5 [6]. The enhanced hemostatic capabilities of TCNF/COL/CS can be ascribed to the synergistic coagulation system, favorable *in vitro* cell compatibility (Fig. 5), extensive porosity (Fig. 3E), large specific surface area (Fig. S3), and stable water absorption system (Figs. 3F and 4) of the aerogel material.

3.6. In vivo hemostatic efficacy

The *in vivo* hemostatic efficacy of these materials was assessed using the liver injury bleeding model (Fig. 7A). Concurrently, a quantitative assessment of the hemostatic efficacy was carried out (Fig. 7B and C). The TCNF/COL/CS material achieved hemostasis within 41 s *in vivo* coagulation tests while the hemostasis time of TCNF/CS, TCNF, and Surgicel® were determined to be 53, 90, and 102 s, respectively. The blood loss for the TCNF/COL/CS sample was quantified as 37 mg, whereas the TCNF/CS, TCNF, and Surgicel® samples showed blood losses of 44 mg, 85 mg, and 98 mg, respectively. The liver damage hemostasis experiment in rats provided further evidence supporting the potent hemostatic effect of TCNF/COL/CS. The blood loss patterns and hemostasis time were congruent and in accordance with the results of the *in vitro* simulation test for coagulation in whole blood (Fig. 6C).

The favorable *in vivo* hemostatic performance of TCNF/COL/CS aerogel can be ascribed to the coagulation properties of CS and COL as well as its noteworthy properties, including high water absorption capacity (Fig. 3F) and high swelling ability (Fig. 4). The hemostatic activity of Surgical® is attributed to its carboxyl content [28]. The exposed carboxyl groups of TCNF aerogel bind with Fe^{3+} of blood through its large pores (Fig. 2) [8]. Both TCNF and Surgicel® have relatively slow hemostatic processes. In contrast, the TCNF/COL/CS aerogel perfectly synergized various pathways to achieve hemostasis. The interconnected pores (Fig. 2) high-water absorption capacity (Fig. 3F) and high swelling ability of TCNF/COL/CS allow it to rapidly absorb blood from the site of bleeding. A large number of pores (Fig. 3E) and high specific surface area (Fig. S3) were used to accelerate contact and concentrate the blood. Finally, in addition to the function of carboxyl groups, CS in the TCNF/COL/CS composite attracted RBCs *via* electrostatic interactions, while COL stimulated platelet activation in human plasma (Fig. 6D), leading to enhanced blood clot formation and promoted rapid hemostasis [56].

Compared with other studies comprised of hemostatic materials such

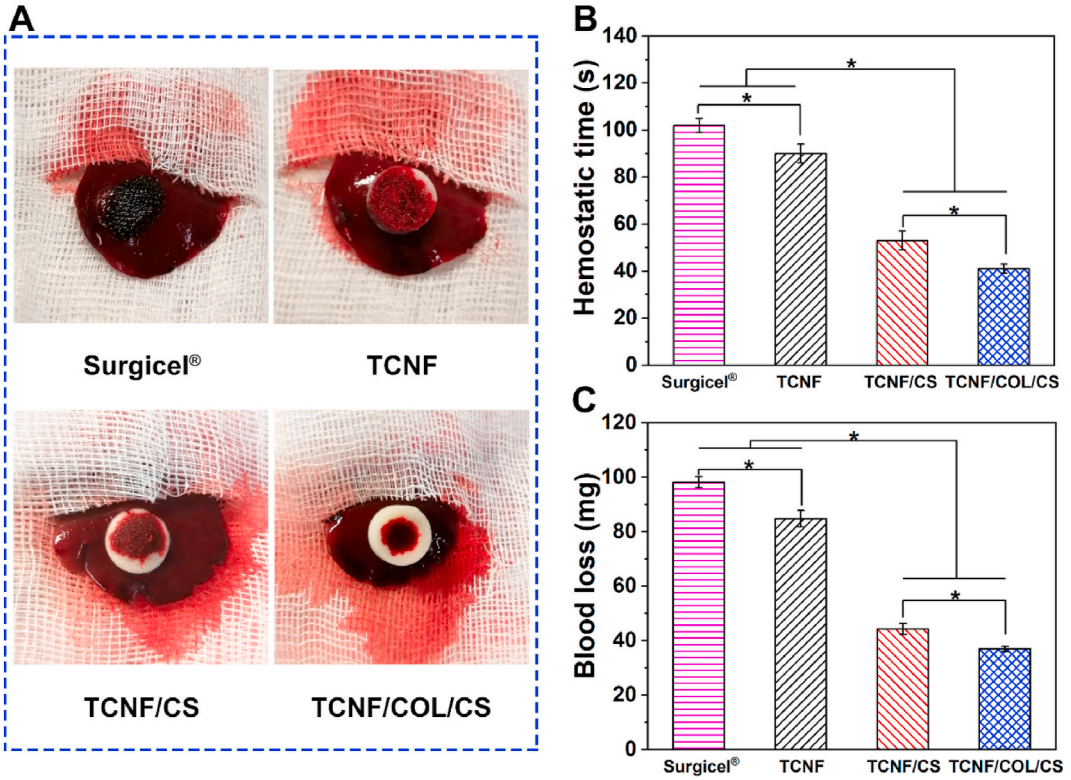

Fig. 7. A rat liver injury model was used to evaluate the hemostatic efficacy of the samples *in vivo*. (A) Images at the macro scale. Hemostatic time and (C) Blood loss quantified within the model. (*$p < 0.05$).

as cellulose or CS [40,57], TCNF/COL/CS demonstrated a higher ability to reduce blood loss in animal models. A hemostatic period of around 1 min was observed with CNF/CSMS, a mixture of CNF and the carboxymethyl chitosan (CMCS) CS derivative; however, it demonstrated blood loss of above 50 mg [57]. Zheng et al. synthesized the hemostasis material SSAD-CSs by combining cellulose nanocrystals doped with the bioactive ingredient *Andrias davidianus* (SSAD) with CNF. In comparison to TCNF/COL/CS, the SSAD-CSs necessitated an extra 26.8 s to achieve hemostasis, resulting in a substantial blood loss of 260.6 mg [40]. Comparatively, TCNF/COL/CS induced a blood loss of 37 mg and a hemostatic time of 41 s in the liver model. The distinguished *in vivo* hemostatic characteristics of TCNF/COL/CS appear to be associated with the following: COL promotes the formation of platelet-induced thrombus, CS enhances RBC aggregation, large internal pores (Figs. 2 and 3E), high capacity for blood absorption and concentration (Fig. 6B and C), and higher *in vitro* cell compatibility (Fig. 5).

3.7. Antibacterial activity

Fig. 8 illustrates the antibacterial properties of the different aerogels. TCNF inhibited the growth of only 78.1 % *E. coli* and 75.2 % *S. aureus*. In contrast, the antibacterial activity of the composite aerogels TCNF/CS and TCNF/COL/CS exceeded 95 % against both strains of bacteria (Fig. 8B), which was considerably greater than that of TCNF.

The observed enhanced antibacterial efficacy of TCNF/COL/CS can be attributed to the incorporation of CS. This is because the positively charged CS interacts electrostatically with the bacterial cell wall, resulting in an uneven distribution of negative charges on the bacteria. The disruption triggers the alterations in bacterial cell membrane, resulting in changes in osmotic pressure and the release of cellular contents, ultimately leading to cell rupture [58]. The developed TCNF/COL/CS aerogel showed positive charges, attributed to the alkali-modified pH resulting from the combination of TCNF with CS (Fig. 3D). The efficient elimination of bacteria can be attributed to the interaction with the charge (Fig. 3D) and the presence of free amino groups on the surface of TCNF/COL/CS aerogel.

The TCNF/COL/CS aerogel showed significantly higher antibacterial activity upon comparison with other cellulose-based materials [59,60]. The citric acid-crosslinked and N-hydroxysuccinimide ester-modified carboxymethyl cellulose aerogel developed by Pan et al., demonstrated 88.2 and 92.9 % killing ratios for *E. coli* and *S. aureus*, respectively [59]. Cheng et al. report that the ORC possesses antibacterial efficacy of 92.9 and 94.7 % against *E. coli* and *S. aureus*, respectively [60]. However, the current study revealed that TCNF/COL/CS showed resistance rates of 95.4 % against *S. aureus* and 96.8 % against *E. coli*, as shown in Fig. 8. The higher antibacterial efficacy of TCNF/COL/CS may be attributed to the incorporation of CS (Fig. 3D). TCNF/COL/CS, a hemostatic aerogel with specific antimicrobial properties, offers potential as a viable filler material for highly infected hemorrhagic wounds (including piercing wounds) or for preventing traumatic infections.

3.8. In vitro and in vivo degradation

Tissue compatibility and degradation capabilities of the samples were evaluated *via in vivo* implantation and *in vitro* material degradation simulation (Fig. 9). The variations of the sample in the degradation simulation experiment are illustrated in Fig. 9B. Following 28 days of *in vitro* degradation, Surgicel®, TCNF, TCNF/CS, and TCNF/COL/CS showed 31, 32.8, 30.6, and 31.3 % weight losses respectively. Fig. 9C illustrates the histocompatibility and *in vivo* degradability of samples with H&E staining. All materials showed an inflammatory response (marked with yellow arrows) with slightly higher *in vivo* degradability

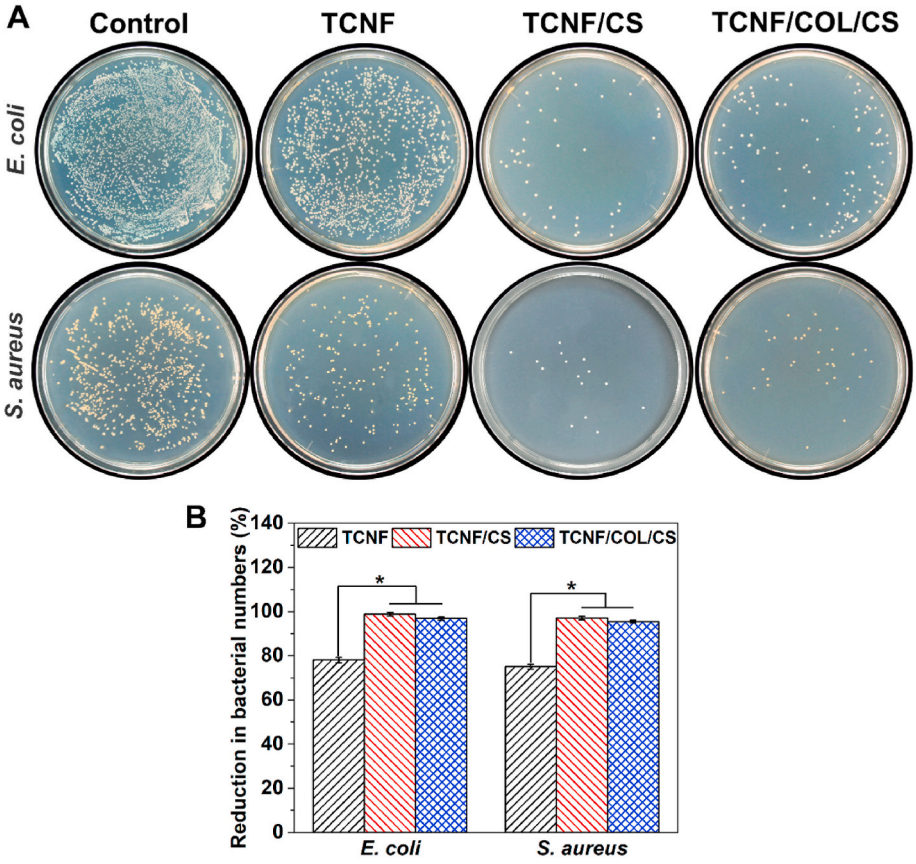

Fig. 8. Antibacterial activities of the samples. (A) Formation of bacterial colonies after incubation with samples. (B) The reduction in bacterial population. (*p < 0.05).

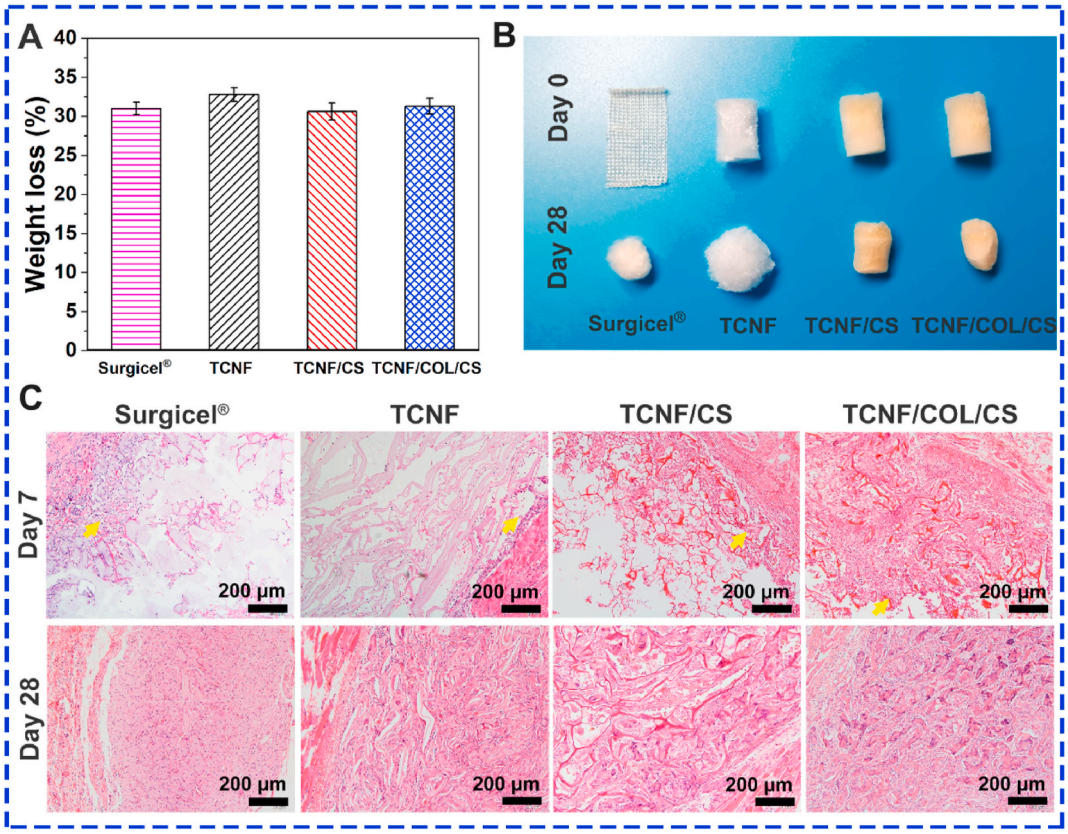

Fig. 9. (A) *In vitro* sample degradation after 28 days. (B) Sample residue after 28 days of PBS degradation. (C) Histopathological assessment of samples using light microscopy following implantation.

than their *in vitro* degradability. TCNF/COL/CS sections exhibit a prominent distribution of inflammatory cells, accompanied by significant fibroblast infiltration into the adjacent tissue. The inflammatory response disappeared in all groups after 28 days. The TCNF/COL/CS demonstrated the most densely packed tissue growth and the highest rate of sample disintegration compared to the other groups. The material showed a loose and fragmented appearance, as evidenced by the progression of tissue cells from its periphery into the interior. The *in vitro* and *in vivo* degradation evaluations revealed the biodegradability of TCNF/COL/CS along with higher biocompatibility and regenerative capacity.

The enhanced biodegradability of TCNF/COL/CS may be attributed to the incorporation of bioactive substances including CS and COL [61,62], the presence of a porous structure, nanofibers, and a larger specific area. As the inflammatory phase decreases, tissue fluid penetrates deeper into the highly porous TCNF/COL/CS (Fig. 3E and F), thereby promoting enhanced surface interaction and contributing to accelerated material degradation. The cells and implanted samples integrated and proliferated, with a significant portion of the material degrading and being replaced by cells. Moreover, COL promoted cell proliferation [63], hence, increasing the penetration of cells into the material. The combined activity of protease, lysozyme, and collagenase *in vivo* led to the rapid degradation of the TCNF/COL/CS aerogel.

In comparison with other cellulose-based materials [42,64], the TCNF/COL/CS aerogel demonstrated a favorable degradation rate *in vitro* and the highest *in vivo* tissue compatibility. The TCNF/CS material developed by Sukul et al., demonstrated an approximate 50 % reduction in weight when exposed to lysozyme *in vitro*. Initially, inflammatory cells were present, followed by a gradual reduction in inflammation and tissue growth within three weeks, indicating that its *in vivo* histocompatibility findings were consistent with the previous research [42]. Queirós et al. conducted a study on OBC hemostatic dressings and observed the presence of inflammatory cells in OBC even 14 days after implantation. A considerable quantity of fibrous components of OBCs remained for 56 days, while the infiltration of fibroblasts into the tissue was restricted [64]. The higher degradation capability and tissue compatibility of TCNF/COL/CS can be attributed to the aerogel's highly porous structure (Figs. 2 and 3E), its efficient water absorption rate (Fig. 3F), superior cell compatibility (Fig. 5), and outstanding blood compatibility (Fig. 6).

4. Conclusions

The TCNF/COL/CS aerogel synergistically combined TCNF, providing antibacterial, hemostatic, and degradation properties, while CS is known for its promising antibacterial effects and ability to aggregate red blood cells. These components were combined *via* electrostatic self-assembly, with the addition of COL, which possesses promising biocompatibility, wound healing capability, and platelet agglutination stimulation, resulting in the formation of a stable sandwich structure. The synthesis of the low-density (15.6 mg/cm^3) TCNF/COL/CS aerogel was achieved without using a cross-linking agent. The aerogel demonstrated a 3D loose structure, high porosity, high water absorption capacity, and medium mechanical strength. The TCNF/COL/CS aerogel, with its interconnecting nanopores, high porosity, and sufficient water absorption capacity, allowed rapid blood absorption, accelerated coagulation, and effective capture of blood components, resulting in quick cessation of bleeding and reduced blood loss. Incorporating bioactive ingredients such as CS and COL enhanced the aerogel's absorption by the organism, histocompatibility, and wound healing capabilities. Moreover, TCNF/COL/CS had significantly enhanced antibacterial capabilities due to the synergetic effect of constituents. Thus, TCNF/COL/CS has significant potential for application in emergency medical care and surgical interventions.

CRediT authorship contribution statement

Lu Liu: Writing – original draft, Visualization, Methodology, Investigation, Formal analysis, Data curation. **Liang Liu:** Writing – original draft, Investigation, Formal analysis. **Lin Chen:** Writing – review & editing, Supervision, Resources, Funding acquisition. **Genqiang Chen:** Writing – review & editing, Supervision, Methodology. **Yen Wei:** Writing – review & editing. **Feng F. Hong:** Writing – review & editing, Supervision, Resources, Methodology, Project administration, Funding acquisition, Conceptualization.

Declaration of competing interest

The authors declare that they have no known competing financial interests or personal relationships that could have appeared to influence the work reported in this paper.

Data availability

Data will be made available on request.

Acknowledgments

Financial support provided by National Advanced Functional Fiber Innovation Center [HX105210640], and State Key Laboratory of Pulp and Paper Engineering [No. 2022010] is gratefully acknowledged. The authors would like to thank all the reviewers who participated in the review.

Appendix A. Supplementary data

Supplementary data to this article can be found online at https://doi.org/10.1016/j.mtbio.2024.101204.

References

[1] S. Pourshahrestani, E. Zeimaran, N.A. Kadri, N. Mutlu, A.R. Boccaccini, Polymeric hydrogel systems as emerging biomaterial platforms to enable hemostasis and wound Healing, Adv Healthc Mater 9 (20) (2020) 2000905, https://doi.org/10.1002/adhm.202000905.

[2] E.M. Shabanova, A.S. Drozdov, A.F. Fakhardo, I.P. Dudanov, M.S. Kovalchuk, V. V. Vinogradov, Thrombin@Fe3O4 nanoparticles for use as a hemostatic agent in internal bleeding, Sci. Rep. 8 (1) (2018) 233, https://doi.org/10.1038/s41598-017-18665-4.

[3] L. Wang, Y. Zhong, C. Qian, D. Yang, J. Nie, G. Ma, A natural polymer-based porous sponge with capillary-mimicking microchannels for rapid hemostasis, Acta Biomater. 114 (2020) 193–205, https://doi.org/10.1016/j.actbio.2020.07.043.

[4] H. Huang, H. Chen, X. Wang, F. Qiu, H. Liu, J. Lu, et al., Degradable and bioadhesive alginatebased composites: an effective hemostatic agent, ACS Biomater. Sci. Eng. 5 (10) (2019) 5498–5505, https://doi.org/10.1021/acsbiomaterials.9b01120.

[5] N. Tartaglia, A. Di Lascia, V. Lizzi, P. Cianci, A. Fersini, A. Ambrosi, et al., Haemostasis in thyroid surgery: collagen-fibrinogen-thrombin patch versus cellulose gauze—our experience, Surg Res Pract 2016 (2016) 3058754, https://doi.org/10.1155/2016/3058754.

[6] H. Yuan, L. Chen, F.F. Hong, A biodegradable antibacterial nanocomposite based on oxidized bacterial nanocellulose for rapid hemostasis and wound healing, ACS Appl. Mater. Interfaces 12 (3) (2020) 3382–3392, https://doi.org/10.1021/acsami.9b17732.

[7] H. Li, W. Cheng, K. Liu, L. Chen, Y. Huang, X. Wang, et al., Reinforced collagen with oxidized microcrystalline cellulose shows improved hemostatic effects, Carbohyd Polym 165 (2017) 30–38, https://doi.org/10.1016/j.carbpol.2017.02.023.

[8] S. Zhang, J. Li, S. Chen, X. Zhang, J. Ma, J. He, Oxidized cellulose-based hemostatic materials, Carbohyd Polym 230 (2019) 115585, https://doi.org/10.1016/j.carbpol.2019.115585.

[9] M.S. Lord, B. Cheng, S.J. McCarthy, M. Jung, J.M. Whitelock, The modulation of platelet adhesion and activation by chitosan through plasma and extracellular matrix proteins, Biomaterials 32 (28) (2011) 6655–6662, https://doi.org/10.1016/j.biomaterials.2011.05.062.

[10] P.M.S. Ouro, D.C.S. Costa, A.J.R. Amaral, J.F. Mano, A supramolecular injectable methacryloyl chitosan-tricine-based hydrogel with 3D printing potential for tissue engineering applications, Macromol. Biosci. 24 (1) (2024) 2300058, https://doi.org/10.1002/mabi.202300058.

[11] X. Fan, Y. Li, X. Li, Y. Wu, K. Tang, J. Liu, et al., Injectable antibacterial cellulose nanofiber/chitosan aerogel with rapid shape recovery for noncompressible hemorrhage, Int. J. Biol. Macromol. 154 (2020) 1185–1193, https://doi.org/10.1016/j.ijbiomac.2019.10.273.

[12] L. Wang, W. Li, Y. Qu, K. Wang, K. Lv, X. He, et al., Preparation of super absorbent and highly active fish collagen sponge and its hemostatic effect in vivo and in vitro, Front Bioeng Biotech 10 (2022) 862532, https://doi.org/10.3389/fbioe.2022.862532.

[13] D. Miranda-Nieves, E.L. Chaikof, Collagen and elastin biomaterials for the fabrication of engineered living tissues, ACS Biomater. Sci. Eng. 3 (5) (2017) 694–711, https://doi.org/10.1021/acsbiomaterials.6b00250.

[14] L. Zheng, S. Zhang, Z. Ying, J. Liu, Y. Zhou, F. Chen, Engineering of aerogel-based biomaterials for biomedical applications, Int. J. Nanomed. 15 (2020) 2363–2378, https://doi.org/10.2147/IJN.S238005.

[15] J. Borges-Vilches, J. Poblete, F. Gajardo, C. Aguayo, K. Fernández, Graphene oxide/polyethylene glycol aerogel reinforced with grape seed extracts as wound dressing, J. Mater. Sci. 56 (28) (2021) 16082–16096, https://doi.org/10.1007/s10853-021-06297-z.

[16] Y. Liu, M. Hao, Z. Chen, S. Ramakrishna, Y. Liu, X. Wang, et al., Recent advances in the development of nanofiber-based aerogel for oil-water separation: a review, Fuel 354 (2023) 129338, https://doi.org/10.1016/j.fuel.2023.129338.

[17] Y. Huang, C. Fan, Y. Liu, L. Yang, W. Hu, S. Liu, et al., Nature-derived okra gel as strong hemostatic bioadhesive in human blood, liver, and heart trauma of rabbits and dogs, Adv Healthc Mater 11 (18) (2022) 2200939, https://doi.org/10.1002/adhm.202200939.

[18] Y. Zhai, C. Gong, J. Chen, C. Chang, Magnetic-field induced asymmetric hydrogel fibers for tough actuators with programmable deformation, Chem Eng J 477 (2023) 147088, https://doi.org/10.1016/j.cej.2023.147088.

[19] X. He, W. Li, S. Liu, Y. Li, Y. Chen, N. Dan, et al., Fabrication of high-strength, flexible, porous collagen-based scaffolds to promote tissue regeneration, Mater Today Bio 16 (2022) 100376, https://doi.org/10.1016/j.mtbio.2022.100376.

[20] L. Chen, M. Subirade, Chitosan/β-lactoglobulin core–shell nanoparticles as nutraceutical carriers, Biomaterials 26 (30) (2005) 6041–6053, https://doi.org/10.1016/j.biomaterials.2005.03.011.

[21] X. Chen, C. Cui, Y. Liu, C. Fan, M. Xiao, D. Zhang, et al., A robust poly(N-acryloyl-2-glycine)-based sponge for rapid hemostasis, Biomater. Sci. 8 (13) (2020) 3760–3771, https://doi.org/10.1039/D0BM00770F.

[22] S. Tang, J. Yang, L. Lin, K. Peng, Y. Chen, S. Jin, et al., Construction of physically crosslinked chitosan/sodium alginate/calcium ion double-network hydrogel and its application to heavy metal ions removal, Chem Eng J 393 (2020) 124728, https://doi.org/10.1016/j.cej.2020.124728.

[23] Z. Chen, Q. Zhang, H. Li, Q. Wei, X. Zhao, F. Chen, Elastin-like polypeptide modified silk fibroin porous scaffold promotes osteochondral repair, Bioact. Mater. 6 (3) (2021) 589–601, https://doi.org/10.1016/j.bioactmat.2020.09.003.

[24] Y. Luo, G. Li, L. Chen, F.F. Hong, Preparation and evaluation of bacterial nanocellulose/hyaluronic acid composite artificial cornea for application of corneal transplantation, Biomacromolecules 24 (1) (2023) 201–212, https://doi.org/10.1021/acs.biomac.2c01052.

[25] M. Shahriari-Khalaji, G. Li, L. Liu, M. Sattar, L. Chen, C. Zhong, et al., A poly-l-lysine-bonded TEMPO-oxidized bacterial nanocellulose-based antibacterial dressing for infected wound treatment, Carbohyd Polym 287 (2022) 119266, https://doi.org/10.1016/j.carbpol.2022.119266.

[26] P. Zhang, L. Chen, Q. Zhang, F. Hong, Using in situ dynamic cultures to rapidly biofabricate fabric-reinforced composites of chitosan/bacterial nanocellulose for antibacterial wound dressings, Front. Microbiol. 7 (2016) 1–15, https://doi.org/10.3389/fmicb.2016.00260.

[27] K.M. Lewis, D. Spazierer, M.D. Urban, L. Lin, H. Redl, A. Goppelt, Comparison of regenerated and non-regenerated oxidized cellulose hemostatic agents, Eur. Surg. 45 (4) (2013) 213–220, https://doi.org/10.1007/s10353-013-0222-z.

[28] Y. Wu, J. He, W. Cheng, H. Gu, Z. Guo, S. Gao, et al., Oxidized regenerated cellulose-based hemostat with microscopically gradient structure, Carbohyd Polym 88 (3) (2012) 1023–1032, https://doi.org/10.1016/j.carbpol.2012.01.058.

[29] H. Maleki, L. Durães, C.A. García-González, P. del Gaudio, A. Portugal, M. Mahmoudi, Synthesis and biomedical applications of aerogels: possibilities and challenges, Adv Colloid Interfac 236 (2016) 1–27, https://doi.org/10.1016/j.cis.2016.05.011.

[30] X. Yu, F. Han, X. Feng, X. Wang, Y. Zhu, C. Ye, et al., Sea cucumber-inspired aerogel for ultrafast hemostasis of open fracture, Adv Healthc Mater 12 (26) (2023) 2300817, https://doi.org/10.1002/adhm.202300817.

[31] H. Yuan, L. Chen, F.F. Hong, Evaluation of wet nanocellulose membranes produced by different bacterial strains for healing full-thickness skin defects, Carbohyd Polym 285 (2022) 119218, https://doi.org/10.1016/j.carbpol.2022.119218.

[32] X. Zhang, I. Elsayed, C. Navarathna, G.T. Schueneman, E.I.B. Hassan, Biohybrid hydrogel and aerogel from self-assembled nanocellulose and nanochitin as a high-efficiency adsorbent for water purification, Acs Appl Mater Inter 11 (50) (2019) 46714–46725, https://doi.org/10.1021/acsami.9b15139.

[33] C. Lai, S. Zhang, X. Chen, L. Sheng, Nanocomposite films based on TEMPO-mediated oxidized bacterial cellulose and chitosan, Cellulose 21 (4) (2014) 2757–2772, https://doi.org/10.1007/s10570-014-0330-3.

[34] Z. Wei, P. Pan, F.F. Hong, Z. Cao, Y. Ji, L. Chen, A novel approach for efficient fabrication of chitosan nanoparticles-embedded bacterial nanocellulose conduits, Carbohyd Polym 264 (2021) 118002, https://doi.org/10.1016/j.carbpol.2021.118002.

[35] A. Barth, Infrared spectroscopy of proteins, Biochim. Biophys. Acta Bioenerg. 1767 (9) (2007) 1073–1101, https://doi.org/10.1016/j.bbabio.2007.06.004.

[36] C. Chen, S. Deng, H. Tian, X. Kou, H. Yu, J. Huang, et al., Novel bioactive sponge mats composed of oxidized bacterial cellulose and chitosan-gum Arabic microcapsules loaded with cinnamon essential oil for enhancing meat preservation, Food Hydrocoll 148 (2024) 109496, https://doi.org/10.1016/j.foodhyd.2023.109496.
[37] N. Hasan, J. Lee, H.-J. Ahn, W.R. Hwang, M.A. Bahar, H. Habibie, et al., Nitric oxide-releasing bacterial cellulose/chitosan crosslinked hydrogels for the treatment of polymicrobial wound infection, Pharmaceutics 14 (1) (2021) 22, https://doi.org/10.3390/pharmaceutics14010022.
[38] K. Meldawati Pasaribu, S. Gea, S. Ilyas, T. Tamrin, I. Radecka, Characterization of bacterial cellulose-based wound dressing in different order impregnation of chitosan and collagen, Biomolecules 10 (11) (2020) 1511, https://doi.org/10.3390/biom10111511.
[39] J. Borges-Vilches, T. Figueroa, S. Guajardo, C. Aguayo, K. Fernández, Improved hemocompatibility for gelatin-graphene oxide composite aerogels reinforced with proanthocyanidins for wound dressing applications, Colloid Surface B 206 (2021) 111941, https://doi.org/10.1016/j.colsurfb.2021.111941.
[40] L. Zheng, Q. Wang, Y.S. Zhang, H. Zhang, Y. Tang, Y. Zhang, et al., A hemostatic sponge derived from skin secretion of Andrias davidianus and nanocellulose, Chem Eng J 416 (2021) 129136, https://doi.org/10.1016/j.cej.2021.129136.
[41] T. Lu, Q. Li, W. Chen, H. Yu, Composite aerogels based on dialdehyde nanocellulose and collagen for potential applications as wound dressing and tissue engineering scaffold, Compos. Sci. Technol. 94 (2014) 132–138, https://doi.org/10.1016/j.compscitech.2014.01.020.
[42] M. Sukul, R.D. Ventura, S.H. Bae, H.J. Choi, S.Y. Lee, B.T. Lee, Plant-derived oxidized nanofibrillar cellulose-chitosan composite as an absorbable hemostat, Mater. Lett. 197 (2017) 150–155, https://doi.org/10.1016/j.matlet.2017.03.102.
[43] F. Cheng, C. Liu, X. Wei, T. Yan, H. Li, J. He, et al., Preparation and characterization of 2,2,6,6-tetramethylpiperidine-1-oxyl (TEMPO)-oxidized cellulose nanocrystal/alginate biodegradable composite dressing for hemostasis applications, ACS Sustain Chem Eng 5 (5) (2017) 3819–3828, https://doi.org/10.1021/acssuschemeng.6b02849.
[44] W. Liu, C. Yang, R. Gao, C. Zhang, W. Ou-Yang, Z. Feng, et al., Polymer composite sponges with inherent antibacterial, hemostatic, inflammation-modulating and proregenerative performances for methicillin-resistant Staphylococcus aureus-infected wound healing, Adv Healthc Mater 10 (22) (2021) 2101247, https://doi.org/10.1002/adhm.202101247.
[45] Y. Chen, Y. Xiang, H. Zhang, T. Zhu, S. Chen, J. Li, et al., A multifunctional chitosan composite aerogel based on high density amidation for chronic wound healing, Carbohyd Polym 321 (2023) 121248, https://doi.org/10.1016/j.carbpol.2023.121248.
[46] H.M.C. Azeredo, L.H.C. Mattoso, R.J. Avena-Bustillos, G.C. Filho, M.L. Munford, D. Wood, et al., Nanocellulose reinforced chitosan composite films as affected by nanofiller loading and plasticizer content, J. Food Sci. 75 (1) (2010) N1–N7, https://doi.org/10.1111/j.1750-3841.2009.01386.x.
[47] M.R. de Moura, M.V. Lorevice, L.H.C. Mattoso, V. Zucolotto, Highly stable, edible cellulose films incorporating chitosan nanoparticles, J. Food Sci. 76 (2) (2011) N25–N29, https://doi.org/10.1111/j.1750-3841.2010.02013.x.
[48] L. Ma, C. Gao, Z. Mao, J. Zhou, J. Shen, X. Hu, et al., Collagen/chitosan porous scaffolds with improved biostability for skin tissue engineering, Biomaterials 24 (26) (2003) 4833–4841, https://doi.org/10.1016/S0142-9612(03)00374-0.
[49] C.R. Kruse, M. Singh, S. Targosinski, I. Sinha, J.A. Sørensen, E. Eriksson, et al., The effect of pH on cell viability, cell migration, cell proliferation, wound closure, and wound reepithelialization: in vitro and in vivo study, Wound Repair Regen. 25 (2) (2017) 260–269, https://doi.org/10.1111/wrr.12526.
[50] Y. Wu, F. Wang, Y. Huang, Comparative evaluation of biological performance, biosecurity, and availability of cellulose-based absorbable hemostats, Clin Appl Thromb-hem 24 (4) (2018) 566–574, https://doi.org/10.1177/1076029617751177.
[51] X. Jia, C. Hua, F. Yang, X. Li, P. Zhao, F. Zhou, et al., Hydrophobic aerogel-modified hemostatic gauze with thermal management performance, Bioact. Mater. 26 (2023) 142–158, https://doi.org/10.1016/j.bioactmat.2023.02.017.
[52] Y. Wang, M. Yin, X. Zheng, W. Li, X. Ren, Chitosan/mesoporous silica hybrid aerogel with bactericidal properties as hemostatic material, Eur. Polym. J. 142 (2021) 110132, https://doi.org/10.1016/j.eurpolymj.2020.110132.
[53] H. Hattori, M. Ishihara, Changes in blood aggregation with differences in molecular weight and degree of deacetylation of chitosan, Biomed Mater 10 (1) (2015) 015014, https://doi.org/10.1088/1748-6041/10/1/015014.
[54] Y. Zhang, Y. Liu, Z. Guo, F. Li, H. Zhang, F. Bai, et al., Chitosan-based bifunctional composite aerogel combining absorption and phototherapy for bacteria elimination, Carbohyd Polym 247 (2020) 116739, https://doi.org/10.1016/j.carbpol.2020.116739.
[55] J. Bian, L. Bao, X. Gao, X. Wen, Q. Zhang, J. Huang, et al., Bacteria-engineered porous sponge for hemostasis and vascularization, J. Nanobiotechnol. 20 (1) (2022) 47, https://doi.org/10.1186/s12951-022-01254-7.
[56] T. Yan, F. Cheng, X. Wei, Y. Huang, J. He, Biodegradable collagen sponge reinforced with chitosan/calcium pyrophosphate nanoflowers for rapid hemostasis, Carbohyd Polym 170 (2017) 271–280, https://doi.org/10.1016/j.carbpol.2017.04.080.
[57] M. Zhou, J. Liao, G. Li, Z. Yu, D. Xie, H. Zhou, et al., Expandable carboxymethyl chitosan/cellulose nanofiber composite sponge for traumatic hemostasis, Carbohyd Polym 294 (2022) 119805, https://doi.org/10.1016/j.carbpol.2022.119805.
[58] P. Feng, Y. Luo, C. Ke, H. Qiu, W. Wang, Y. Zhu, et al., Chitosan-based functional materials for skin wound repair: mechanisms and applications, Front. Bioeng. Biotechnol. 9 (2021), https://doi.org/10.3389/fbioe.2021.650598.
[59] S. Pan, Y. Li, X. Tong, L. Chen, L. Wang, T. Li, et al., Strongly-adhesive easily-detachable carboxymethyl cellulose aerogel for noncompressible hemorrhage control, Carbohyd Polym 301 (2023) 120324, https://doi.org/10.1016/j.carbpol.2022.120324.
[60] F. Cheng, J. He, T. Yan, C. Liu, X. Wei, J. Li, et al., Antibacterial and hemostatic composite gauze of N,O-carboxymethyl chitosan/oxidized regenerated cellulose, RSC Adv. 6 (97) (2016) 94429–94436, https://doi.org/10.1039/C6RA15983D.
[61] G.I. Howling, P.W. Dettmar, P.A. Goddard, F.C. Hampson, M. Dornish, E.J. Wood, The effect of chitin and chitosan on the proliferation of human skin fibroblasts and keratinocytes in vitro, Biomaterials 22 (22) (2001) 2959–2966, https://doi.org/10.1016/S0142-9612(01)00042-4.
[62] Z. Zheng, M. Li, P. Shi, Y. Gao, J. Ma, Y. Li, et al., Polydopamine-modified collagen sponge scaffold as a novel dermal regeneration template with sustained release of platelet-rich plasma to accelerate skin repair: a one-step strategy, Bioact. Mater. 6 (8) (2021) 2613–2628, https://doi.org/10.1016/j.bioactmat.2021.01.037.
[63] M. Zheng, X. Wang, Y. Chen, O. Yue, Z. Bai, B. Cui, et al., A review of recent progress on collagen-based biomaterials, Adv Healthc Mater 12 (16) (2023) 2202042, https://doi.org/10.1002/adhm.202202042.
[64] E. Queirós, S. Pinheiro, J. Pereira, J. Prada, I. Pires, F. Dourado, et al., Hemostatic dressings made of oxidized bacterial nanocellulose membranes, Polysaccharides 2 (2021) 80–99, https://doi.org/10.3390/polysaccharides2010006.